Energy and AI 15 (2024) 100309

Contents lists available at ScienceDirect

Energy and AI

journal homepage: www.sciencedirect.com/journal/energy-and-ai

VISION-iT: A Framework for Digitizing Bubbles and Droplets

Youngjoon Suh [a], Sanghyeon Chang [a], Peter Simadiris [a], Tiffany B. Inouye [a], Muhammad Jahidul Hoque [c], Siavash Khodakarami [c], Chirag Kharangate [d], Nenad Miljkovic [c,e,f,g], Yoonjin Won [*,a,b]

[a] Department of Mechanical and Aerospace Engineering, University of California, Irvine, 4200 Engineering Gateway, CA 92617-2700, USA
[b] Department of Electrical Engineering and Computer Science, University of California, Irvine, 5200 Engineering Hall, CA 92617-2700, USA
[c] Department of Mechanical Science and Engineering, University of Illinois at Urbana-Champaign, Urbana, IL 61801, USA
[d] Mechanical and Aerospace Engineering Department, Case Western Reserve University, Cleveland, OH, 44106, USA
[e] Department of Electrical and Computer Engineering, University of Illinois at Urbana-Champaign, Urbana, IL, 61801, USA
[f] Materials Research Laboratory, University of Illinois at Urbana-Champaign, Urbana, IL, 61801, USA
[g] International Institute for Carbon Neutral Energy Research (WPI-12CNER), Kyushu University, 744 Moto-oka, Nishi-ku, Fukuoka 819-0395, Japan

HIGHLIGHTS

- A vision-based deep learning framework is developed to systematically study two-phase nucleation dynamics from a data-centric standpoint.
- Identifying detection- and tracking-level errors is critical to ensure high-quality two-phase nucleation feature extractions.
- Optimized detection and tracking parameters are defined through semi-automated image annotations specific examples.
- Performance metrics are evaluated over a wide spectrum of heat fluxes to ensure optimal quantification of varying two-phase nucleation dynamics.

GRAPHICAL ABSTRACT

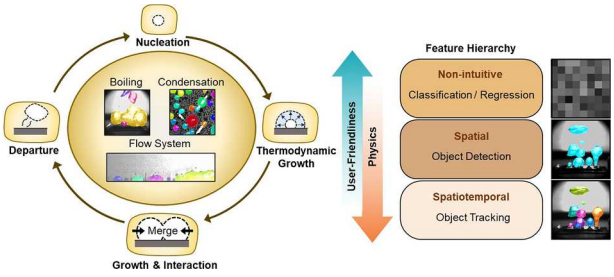

ARTICLE INFO

Keywords:
Deep learning
Computer vision
Nucleation
Heat transfer
Phase-change phenomena

ABSTRACT

Quantifying the nucleation processes involved in liquid-vapor phase-change phenomena, while dauntingly challenging, is central in designing energy conversion and thermal management systems. Recent technological advances in the deep learning and computer vision field offer the potential for quantifying such complex two-phase nucleation processes at unprecedented levels. By leveraging these new technologies, a multiple object tracking framework called "vision inspired online nuclei tracker (VISION-iT)" has been proposed to extract large-scale, physical features residing within boiling and condensation videos. However, extracting high-quality features that can be integrated with domain knowledge requires detailed discussions that may be field- or case-specific problems. In this regard, we present a demonstration and discussion of the detailed construction, algorithms, and optimization of individual modules to enable adaptation of the framework to custom datasets. The concepts and procedures outlined in this study are transferable and can benefit broader audiences dealing with similar problems.

* Corresponding author.
E-mail address: won@uci.edu (Y. Won).

https://doi.org/10.1016/j.egyai.2023.100309

Available online 18 October 2023

1. Introduction

Liquid-vapor phase-change phenomena are critical for maintaining a sustainable and habitable environment on Earth. These phenomena continue to play a central role in present-day industries with ever growing presence. Phase-change processes utilize the high latent heat of the working fluid to transport great amounts of thermal energy efficiently [1]. Among various phase-change processes, boiling and condensation are two of the most widely used in both domestic and industrial applications [2]. Therefore, increasing the heat transfer efficacy of these processes can bring transformational changes to the safety, durability, cost, and sustainability of thermal energy systems [2].

Despite its significance and widespread usage, the underlying mechanisms governing boiling or condensation heat transfer performances can be elusive and are still considered by some as technologies yet to mature [3]. Over more than a century, extensive research has been conducted to maximize phase-change heat transfer performances through theoretical and computational modeling [4], surface engineering [5–7], new metrologies [8–10], and a diverse set of experimental conditions [11,12]. The accumulated data has led to a multitude of both empirical and phenomenological correlations that have become the building blocks of the two-phase heat transfer field. However, many of these correlations are narrowly restricted to a specific range of conditions, geometries, and working fluids, which ultimately contribute to the high level of data inconsistency present today.

One of the primary reasons for inconsistencies in boiling and condensation studies is due to the poor understanding of and weak connection between nucleation statistics and effective heat and mass transport performances. Boiling and condensation are both quasi-steady processes [13], involving a temporal sequence of secondary phase (i.e., bubbles for boiling and droplets for condensation) nucleation, growth, interaction, and departure (Fig. 1a). Nucleation parameters, such as nuclei growth rate, nucleation site density, departure frequency, and departure diameter, have been instilled in traditional two-phase heat and mass transfer models for decades, but many of these parameters are derived from small quantities of manually extracted empirical datasets [14]. The need for better connections between experiments and visualization methods has become increasingly important over the years as classical nucleation dynamics using different conditions have begun to deviate from what researchers previously understood as the norm [11,15]. To address this challenge, it is imperative to take a data-driven approach by extracting, curating, and analyzing mass nucleation information from chaotic two-phase processes. One of the most viable and straightforward solutions is to analyze information-rich imagery (i.e., images and videos) that continues to be a customary part of most boiling and condensation experiments [16].

However, analyzing image data continues to be a daunting challenge for researchers. A significant portion of studies still rely on time-consuming and labor-expensive manual image analysis [16]. Algorithmic computer vision approaches, such as thresholding and edge detection, are popular methods that have been used to analyze images over the past two decades. However, these approaches require significant environmental control, and they can perform poorly with even slight changes in lighting or contrast [17–19]. Recently, machine learning and deep learning techniques have emerged as powerful tools for performing digital inference tasks [16,20,21]. Unlike traditional algorithmic approaches that rely heavily on handcrafted features and carefully designed experimental settings, machine learning and deep learning models are trained, rather than programmed, and therefore outperform other methods [22].

Digital inference enables the acquisition of meaningful and rich physical descriptors through a feature hierarchy shown in Fig. 1b. At the bottom of the hierarchy, neural networks are designed and trained to learn salient features, such as edges, brightness, contrasts, and contours, from images. These features are typically used in modern deep learning models that address classification or regression problems. Previous examples of machine learning tasks include identifying different stages of the heat transfer curve [23], detecting nucleation behavior anomalies [24], and even forecasting events [25].

To extract physically meaningful information from the digital inference process, it is necessary to refine the process through object detection [26]. The object detection task allows to extract specific

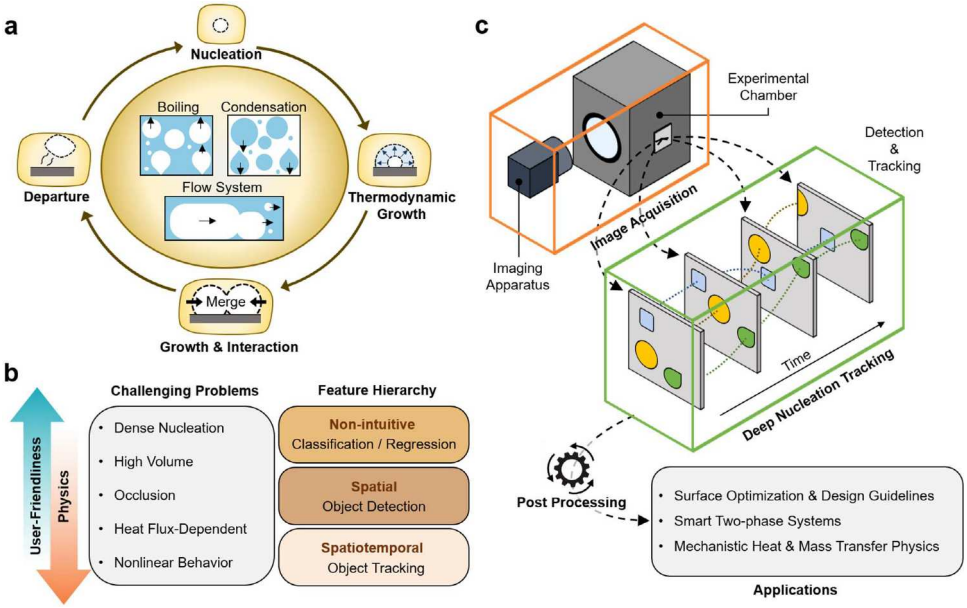

Fig. 1. Applications of vision-inspired online nuclei tracker (VISION-iT) for phase-change heat transfer analysis. (a) Phase-change processes follow nucleation, growth, interaction, and departure cycles, which can consist of hundreds of nucleation instances per second. (b) Artificial Intelligence (AI) solutions towards overcoming challenging two-phase image analysis come with varying feature levels. At the higher end of the feature hierarchy, spatio-temporal feature extractors are generally less user-friendly because they consist of multiple modules. (c) VISION-iT passes collected image data (from the orange frame) through object detection, tracking, and data processing modules (green frame) to extract multi-level physical descriptors that will establish a holistic description of two-phase heat and mass transfer.

features with varying levels of complexity, ranging from bounding box-level to pixel-level accuracy. At the most basic level, the networks specify the type, rough size, and location of objects via bounding box (bbox) regression [27,28]. With more advanced models, objects can be entirely segmented from the background with pixel-level accuracy [29]. While object detection modules can explain various aspects of *in situ* bubble or droplet dynamics, the most informative features are spatio-temporal, meaning that detected objects must also be linked with time information, which might be challenging.

Our group has recently reported a vision-based framework named vision-inspired online nuclei tracker (VISION-iT), which can autonomously curate millions of informative physical descriptors from dense nucleation activity using video data (Fig. 1c) [21]. VISION-iT has proven to be essential in the retrospective analysis of heat and mass transfer and monitoring of nuclei behavior during phase-change. However, the framework consists of multiple integrated components which must be carefully customized to different nucleation conditions for optimal performance. Therefore, the practical challenges of applying VISION-iT to custom datasets include a concrete understanding of domain-specific nuclei behaviors, the recognition of the various sources of errors involved in each module, and the comprehensive physical description of two-phase heat transfer parameters.

In this work, we demonstrate the operational procedures of VISION-iT by taking the example from pool boiling. We begin by providing detailed methods to quantitatively validate the performance of VISION-iT, including custom-defined validation metrics. Then, we identify common errors related to individual components of the framework and propose strategies to minimize them. Finally, the framework discussed in this study can be expanded to other applications within and beyond the thermal sciences through practical examples. The framework can be useful to analyze nucleation-based processes, such as boiling, condensation, frosting, icing, cell-adhesion, crystal formation, corrosion, and flow analysis.

2. Results

2.1. Overall framework

VISION-iT is an integrated pipeline consisting of image acquisition, instance-level object detection, object tracking, and post processing modules fine-tuned for, but not limited to, bubble and droplet feature extraction. At the image acquisition stage, high resolution optical images are collected from experimental apparatus. The object detection module then uses a custom-trained Mask R-CNN model to perform instance segmentation, where pixel-wise masks bearing unique identifiers (IDs) are generated for individual objects (i.e., droplet or bubble) in each frame (see Methods Section and Supplementary Materials S1 for the detailed training procedure). An object tracking module takes the detected masks and passes them through a TrackPy-based cell tracking package [30,31], where the IDs are linked with respect to time. Finally, a data processing module post-processes the datasets to filter objects clipped by the view field and extract high-level spatio-temporal features.

2.2. Detection- and Tracking-level errors

To provide a holistic description of multi-level features, it is crucial to understand, prevent, and mitigate errors that manifest themselves within each module (Fig. 2). Errors arising from multiple-object tracking (MOT) module can be largely categorized into detection-level errors (where the primary concern is to accurately locate multiple objects in an image) and tracking-level errors (where the goal is to maintain correct object IDs and yield their respective trajectories throughout the sequence of images).

Detection-level errors are mainly governed by the difficulties associated with representing three-dimensional nucleation phenomena by using two-dimensional images. For example, a common error associated with pool boiling is occlusion-induced errors (OIEs), or errors that arise when an object is fully or partially hidden by another object of the same class, such as a bubble, situated closer to the camera (Fig. 2a). Moreover,

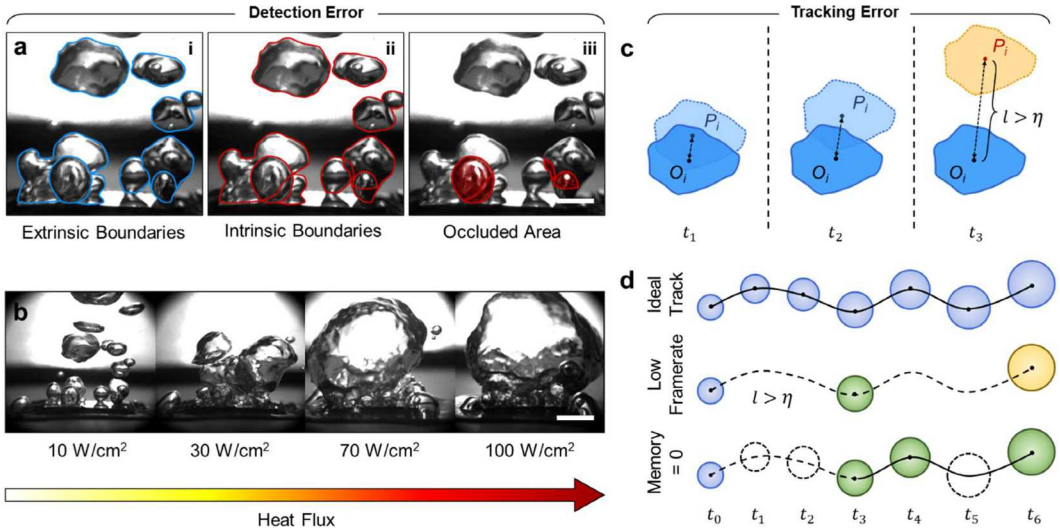

Fig. 2. Detection and tracking errors from the VISION-iT framework. (a) At the object detection level, the morphological diversity of objects poses difficulties in identifying individual instances. Occlusions are often observed and can cause underestimations of the object size. For example, the comparison between extrinsic boundaries (blue) and the estimated intrinsic boundaries (red) results in missing occluded areas (shaded). The scale bar represents 3 mm. (b) Model performances may vary depending on the difficulty of the visual scenes. For example, nucleation activities can drastically vary depending on the heat flux of the surface and cause performance deviations. The scale bar represents 3 mm. Following the object detection, tracking parameters such as search range threshold η and memory ψ dictate the tracking performances. (c) The illustration shows that when the distance l between an object O_i and prediction P_i exceeds a certain search range threshold η, the model can no longer make a correspondence and switches the ID (color). (d) Ideally, the object detector will identify all objects throughout the given timeframes. The memory of the model decides the maximum number of frames for which a feature can vanish and then reappear nearby, and still be considered the same particle. The figure illustrates an ideal track, a track at low framerates where all objects are detected, and a track where the model misses objects at time t_1, t_2, and t_5. On the third track, the model loses object correspondence when memory is set to 0. Note that the same type of errors can occur when using a low framerate because the search range threshold η is exceeded.

performance deviations can be introduced when predicting for varying bubble dynamics (Fig. 2b), which have a proclivity to change when experimental parameters such as heat flux, surface chemistry, surface architecture, orientation, and working fluid are changed [13,32]. Therefore, it is important for the model to generalize well across a wide range of nucleation and departure behaviors. In both cases, the errors must be quantified by the researcher to assess the prediction performance of the model.

Tracking-level errors are inevitably subject to the performance of the object detection model but can be mitigated by adjusting parameters in the linking module. The goal of the linking step is to find the most suitable set of assignments that match each feature in the previous frame with the corresponding feature in the current frame. While the most recent location of the object is a good candidate for matching features between frames, the nearest distance does not always result in correct pairing [30]. This is especially true for boiling and condensation processes where new nuclei spontaneously form close to each other. Therefore, the tracking module links features using spatial coordinates as well as other instance characterizations available in the scikit-image toolkit such as eccentricity, perimeter, equivalent diameter, orientation, and solidity [33]. The tracking module then exploits an extended Crocker-Grier algorithm to link features together [34] using variables such as "search range" η, "memory" ψ, and feature weights to conserve computing power and time [30].

Search range, η, refers to a physical circular domain, centered on the most likely new position of an object, that the module will restrict its search to. As illustrated in Fig. 2c, the correspondence between object O_i and the prediction P_i is lost if their distance l exceeds the search range threshold η where i is the instance. In other words, using a small η can considerably increase the speed of the linkage process, but comes at the expense of losing the trajectories of objects for which $l > \eta$. Therefore, ideally η should be larger than the largest displacement of any object between frames, but smaller than the smallest distance between any two objects. However, the chances of having boiling and condensation videos in which these two distances are always distinct are slim. Depending on the framerate or the maximum velocity of bubbles or droplets, the maximum displacement varies greatly across different heat fluxes, as depicted in Fig. 2b, requiring different η values for each heat flux step. To address this issue, an "adaptive search" functionality is employed to allow for the tracking module to select candidate features more intelligently by starting with a maximum η and automatically reducing it when and where the model encounters difficulty [30].

Memory, ψ, is a parameter that controls the maximum number of frames in which an object can vanish and still be considered as the same object (Fig. 2d). Due to the complexity associated with two-phase system [16,35], objects occasionally vanish for a small number of frames due to occlusions (Fig. 2a) and flickering predictions [36]. Accordingly, ψ becomes an important parameter to keep accurate track of bubbles generated during pool boiling. However, setting ψ to be too high, and thus reaching back too far, can have negative effects by not recognizing new bubbles originating from a new nucleation cycle. The effects of acquiring images with low framerates and using low ψ are elucidated in Fig. 2d. While both cases can capture fragments of the object's history throughout time, the tracker loses the object ID due to restricted spatial search range for the low framerate case and limited temporal search range for small ψ case.

Finally, the model can use different weights to allow the tracker to link objects based on specific nucleation characteristics such as vertical or lateral movements. For example, during atmospheric pool boiling, bubbles are forced to rise due to buoyancy, establishing a difficult case where bubbles with similar shapes and sizes exist close to one another in both x and y directions. By adding weight to the x coordinate feature, the tracker has a greater tendency to link objects that are laterally closer in successive frames. Since the change in the x coordinate of a rising bubble is rarely larger than the distance between two bubbles being side by side in consecutive timesteps, the tracker is effectively forced to link rising bubbles. Similar strategies can be applied to other nucleation-based flow systems if they have preferable orientations. For example, it could be more advantageous to add weight to the spatial coordinates and object size for a dense coverage of identically shaped droplets [20]. Table S1 provides a detailed list of the models and weights discussed in this study.

2.3. Validation metrics

Evaluating MOT performances is a nontrivial task, which requires the rigorous characterization of both detection- and tracking-level performances. This study showcases the predictive performance of VISION-iT for pool boiling videos for demonstrative purposes. All evaluation metrics are grounded on at least 250 manually labeled, sequential images (i.e., groundtruth (GT) per heat flux increment adding to a total of >1250 images. These datasets are used for evaluation purposes only and not for object detection model training. See the Methods Section for detailed annotation procedures.

At the detection stage, we assess the tailored Mask R-CNN model ability to segment bubbles into pixelwise masks using standard evaluation metrics as well as custom-defined metrics. Standard evaluation metrics, such as recall, precision, accuracy, and F-1 score, evaluate the segmentation performance through different combinations of possible outcomes of predicted instances (Fig. 3a). A true positive (TP) is defined as a condition when the model correctly detects an existing object that matches the GT, and a false positive (FP) is counted when the model labels or categorizes an image when it should not have. Conversely, a true negative (TN), although rare, situates when the model correctly predicts that there are no instances within the image. Finally, a false negative (FN) is assigned when the model misses an object with respect to the GT.

In previous work where performance metrics were calculated based on IoU thresholds, the models were shown to maintain high-level performance >90 % until tight IoU thresholds >0.9 were implemented [21]. Here, we implement stricter standards by determining positive- and negative-conditioned pixels instead of IoU thresholds. According to their respective definitions [37]:

$$\text{Recall} = \frac{\sum TP}{\sum (TP + FN)}, \tag{1}$$

$$\text{Precision} = \frac{\sum TP}{\sum (TP + FP)}, \tag{2}$$

$$\text{Accuracy} = \frac{\sum (TP + TN)}{\sum (TP + TN + FN + FP)}, \tag{3}$$

and

$$F-1 \text{ score} = 2 \cdot \frac{\text{Precision} \cdot \text{Recall}}{\text{Precision} + \text{Recall}}. \tag{4}$$

In addition to these performance metrics, a metric called mean average pixel error (MAPE) evaluates the model prediction accuracy at the pixel-level (Fig. 3b). For this, the pixelwise error (PE) can be calculated by subtracting the GT and predicted mask (PM) images:

$$PE_j = GT_j - PM_j, \tag{5}$$

where an image j. Then, the MAPE is calculated by dividing each PE by its respective GT:

$$\text{MAPE} = \frac{1}{n} \sum_{j=1}^{n} \left| \frac{PE_j}{GT_j} \right| \cdot 100 \tag{6}$$

for the total n images.

In parallel to MAPE, we quantify errors caused by bubble-bubble occlusions (i.e., OIE) by dividing pixel-based occlusion errors (OEs) with the GT:

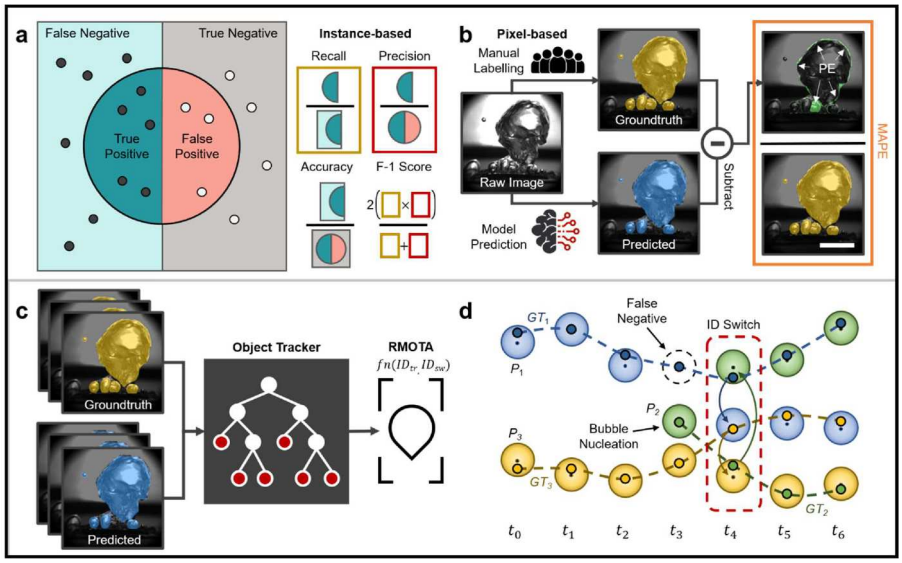

Fig. 3. Object detection and tracking validation metrics. (a) Illustration of traditional detection metrics such as recall, precision, accuracy, and F-1 score. (b) Schematic of workflow for determining mean average pixel error (MAPE). (c) Relative multiple-object tracking accuracy (RMOTA) is calculated by comparing the extent that predicted mask videos deviate from the ground truth, *GT*. (d) Representative examples of ID mismatches that can occur during object tracking. The small circles with dotted lines represent the ground truths, GT_i, whereas colored circles indicate predictions, P_i. In the frames from t_0 to t_2, P_1 and P_3 are correctly mapped to their respective *GT*s. At t_3, P_2 first appears, P_1 disappears, and P_3 is situated close to P_2. The combination of such events causes all IDs to switch at t_4.

$$\mathrm{OIE} = \frac{1}{n}\sum_{j=1}^{n}\left|\frac{OE_j}{GT_j}\right|\cdot 100 \tag{7}$$

To determine OEs (Fig. 2a-iii), a minimum of 200 images having occlusion events are separately labelled per dataset, where the intrinsic boundary estimations are added into the GT as shown in Fig. 2a-II.

At the tracking stage, we define a metric called relative multiple-object tracking accuracy (RMOTA) to evaluate the tracking performance of complex systems where the tracking groundtruth may be unavailable, or impractical to generate. Despite the growing interest in using object tracking for academic and commercial purposes, there is still no clear golden standard for evaluating the tracking quality [38,39]. Moreover, the evaluations are conducted on official datasets with identical GTs, which suggests that even the best model may not perform well on custom datasets. The difficulty of assessing the tracking performance on custom datasets varies significantly depending on the application at hand. For instance, creating GT tracks for complex systems that display chaotic behavior, such as boiling, is notoriously difficult because it demands general solutions for highly subjective problems. One such example is tracking IDs for bubbles during their merging events. Furthermore, in high nucleation density systems such as condensation, it is practically impossible to manually track every droplet for a large number of frames. To address these challenges, we propose RMOTA (see Supplementary Materials S2 for a detailed derivation), which compares the relative tracking performance between input videos of predicted masks and GT masks (Fig. 3c):

$$\mathrm{RMOTA} = 1 - \frac{\sum_t (ID_{tr} + ID_{sw})_j}{\sum_t (GT)_j}, \tag{8}$$

where ID_{tr} is the difference between the number of tracked IDs per frame, and ID_{sw} is the number of ID switching events relative to the GT with respect to image *j*. RMOTA is a relative measure of how well the model tracks objects, comparing object masks predicted by Mask R-CNN to manually labeled (i.e., GT) object masks. RMOTA assumes that the trajectories created from manually labeled objects are ideal because they minimize mispredictions or missing objects. Under this definition, RMOTA incorporates errors resulting from missed objects as well as ID switching events. Fig. 3d illustrates an example case of where ID switching events can lead to completely misinterpreted tracks, where dashed lines represent the GT paths, and predictions *P* are color-coded based on how the model linked them over time. At t_4, the combination of the initialization and termination of tracks, similar morphology, and dense packing leads to all three instances switching their IDs. Furthermore, because the object linkage process is influenced by η and ψ, RMOTA optimization involves a series of iterations until it meets the appropriate criteria (RMOTA > 75%) across all heat fluxes.

2.4. Detection module optimization

To assess the detection model across varying heat fluxes (4 – 50 W/cm^2), we employ instance-based or pixel-based metrics as well as occlusion errors, as shown in Figs. 4a-c. The model scores exceptionally well (> 83 %) on conventional instance-based metrics, such as accuracy, recall, F-1 score, and precision across all tests. In comparison to precision, the model scores relatively high in recall, which implies that the model leans towards missing objects rather than mislabeling them (Fig. 4a). Overall, the model scores higher at the low (4 W/cm^2) and high (50 W/cm^2) heat fluxes, respectively. We speculate this to be a result of bubbles having a varying level of difficulties between the low- and high-end of the heat flux spectrum. On the one hand, bubbles forming near the onset of nucleate boiling (ONB) form as isolated bubbles with minimum bubble-bubble interaction. On the other hand, bubbles are ejected as a singular unit at high (> 50 W/cm^2) heat fluxes due to elevated nucleation density paired with rapid bubble coalescence. The intermediate regime (14 – 31 W/cm^2) poses the greatest challenge for all vision-based analysis because it is fraught with chain interactions that are difficult to distinguish, even for a trained expert.

Similar to the instance-based metrics, the pixel-based errors including MAPE and OIE also show low (< 6 %) values for all heat fluxes, which can be negligible (Fig. 4b and c). In alignment with our hypothesis, the MAPE peaks at an intermediate heat flux of 23 W/cm^2 and decreases as the heat flux further increases. Meanwhile, OIE exhibits a continuously increasing trend as the heat flux increases, suggesting that occlusion errors become more pronounced as the overall bubble size grows.

To maximize detection fidelity, researchers should optimize imaging

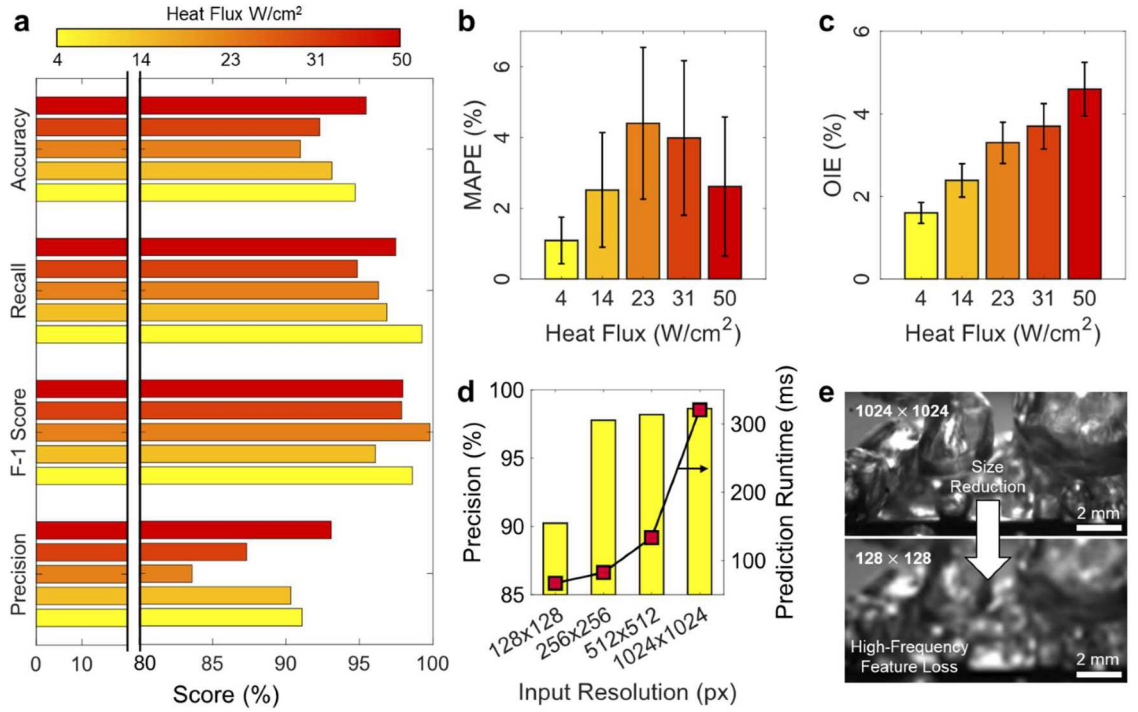

Fig. 4. Object detection results. (a) Plot showing how a custom-trained model performs on a wide heat flux range (4 – 50 W/cm^2). (b) The MAPE and (c) occlusion-induced error (OIE) both show reasonably low values, < 6 %, confirming the pixel-wise accuracy of the trained model. (d) The results show an inherent trade-off between precision (yellow bars) and prediction runtime (red squares) for varying image sizes, where precision and inference time suffer greatly when image dimensions are too small or too large, respectively. (e) The reduction of image dimensions from 1024 × 1024 pixels to 128 × 128 pixels cause high-frequency feature loss, which is detrimental for both object detection training and prediction.

conditions, image quality, and annotation consistency. Although there is a pressing demand for a foundation model tethered to two-phase nucleation applications, such models would require a collaborative effort among different institutes to enable access to a wide range of image datasets to train on. Therefore, it is currently still more practical to fine-tune deep learning algorithms to the specific experimental environment.

With this in mind, we first recommend maintaining relatively controlled visualization environments by minimizing unnecessary errors that can come from operations. Although deep learning-based computer vision models respond better to environmental changes than traditional computer vision algorithms [20], it is still advantageous to reduce potential errors caused by preventable vibration or illumination variation. Furthermore, since a consistent pixel-to-length conversion is crucial for accurate measurements, it is convenient to maintain a fixed focal length throughout all experiments to efficiently cross-compare evolving bubble dynamics between differing heat fluxes and surfaces.

The image quality is an important factor that determines whether the image is analyzable. Bubbles or droplets captured at low framerates become distorted due to motion blur, which might not be suitable for further analysis such as labeling. In addition, relatively large 2D boiling surface areas can produce an excessive number of bubbles such that either the bubbles outside the focal view become blurred, or intra-class occlusion events become overwhelming. The errors associated with this these cases can be reduced by collecting pool boiling images from smaller boiling surfaces or 1D line heaters. Finally, detection-level errors can be further reduced by enhancing the consistency of annotations. This study minimizes human-induced annotation errors by developing a human-in-the-loop annotation framework (see Supplementary Materials S1 and Fig. S1) that realizes semi-automatic image annotations in addition to demonstrating clear annotation rules (see Table S2) along with active communication between annotators.

Finally, we report a resolution-induced trade-off between accuracy and prediction time when inferring imaging data. Fig. 4d quantifies this conflict, showing a considerable prediction runtime difference of 131 % when comparing a 128 × 128 to a 1024 × 1024 pixel case. The discrepancy is caused by high-frequency feature loss, as shown in Fig. 4e, where high-pixel intensity variations are smoothened from file compression. To make the balance between accuracy and computational time, this study employs 512 × 512 pixel images.

2.5. Tracking module optimization

Enhancing the tracking module involves multiparametric fine-tuning of linkage specifications and weights. However, quantitatively assessing the tracking performance is a major challenge for most two-phase processes due to limited access to the GT videos. To address this challenge, we introduce a semi-automatic workflow to derive the best tracking conditions, as listed in Fig. 5a. To begin, an initial set of tracking parameters (i.e., η and ψ) and weights are selected for manual initial validation. Typically, poor linkage can be quickly filtered by monitoring incomplete tracks and ID switches. If the linkage process passes manual screening, the present weights are fixed for all heat flux steps. The tracking parameters η and ψ are then fine-tuned by mapping RMOTA, as shown in Fig. 5b, where maximum values are denoted with an asterisk. The results show that RMOTA drastically declines when $\eta < 135$ is applied. Furthermore, the combination of $\eta = 135 - 225$ and $\psi = 2 - 3$ offers the best tracking performance for our examples of pool boiling. Fig. 5c compares the tracking performance when different weights are applied, confirming that fine-tuning can assist with the optimization of specific tasks.

3. Discussion

As ML-assisted frameworks become increasingly popular in the thermal science community, the impact of big and new data is becoming more pronounced. The VISION-iT framework addresses one of the enduring challenges of acquiring a sufficient amount of high-quality

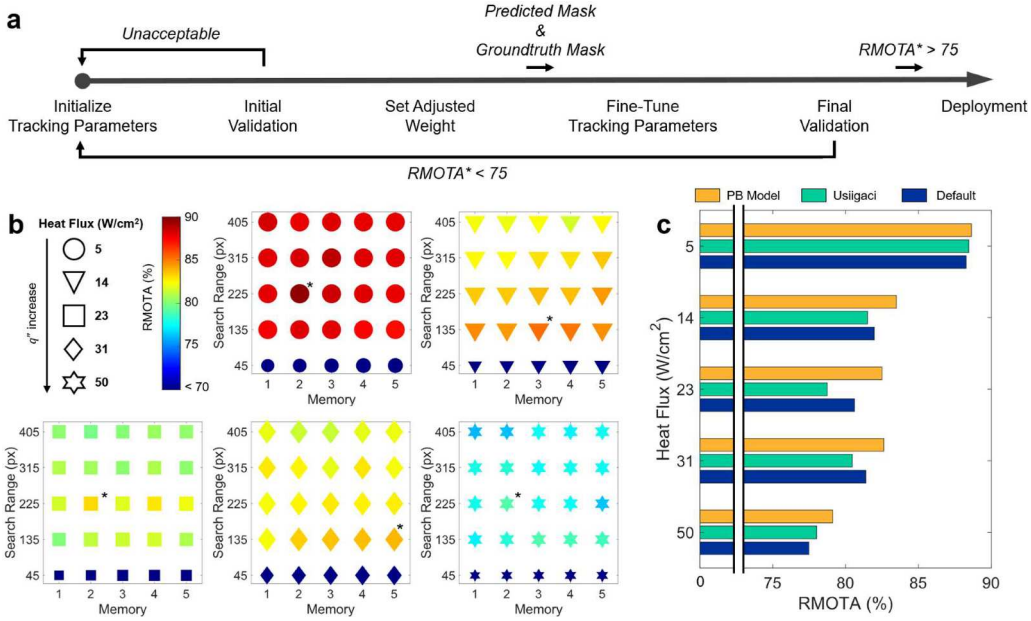

Fig. 5. Object tracking statistics. (a) The tracker optimization procedure follows an iterative process until the target RMOTA is obtained. (b) Tracking parameters are fine-tuned by mapping the search range η and memory ψ with respect to RMOTA. The plot shows a representative mapping of η and ψ using adjusted weights. The model with the highest performance is marked with an asterisk. (c) Parameters adjusted for pool boiling applications show high RMOTA scores compared to other models.

data during nucleation dynamics. The VISION-iT framework can be adapted for various applications (Fig. 6) and provide a detailed description of the algorithms used (See Supplementary Materials S3). For example, VISION-iT can extract classic nucleation dynamics parameters, such as departure diameter (Fig. 6b), nucleation site density (Fig. 6c), and departure frequency (Fig. 6d), over the full boiling curve during pool boiling [40]. In addition, our recent work demonstrates ultra-high resolution surface heat flux mapping capabilities during dropwise condensation experiments (Fig. 6e – g) with up to 300 nm and 200 ms spatio-temporal resolutions, respectively [20]. Moreover, we demonstrate that the same methods can be applied to condensation tests where surface patterns, similar to droplet morphologies, exist (Fig. 6e).

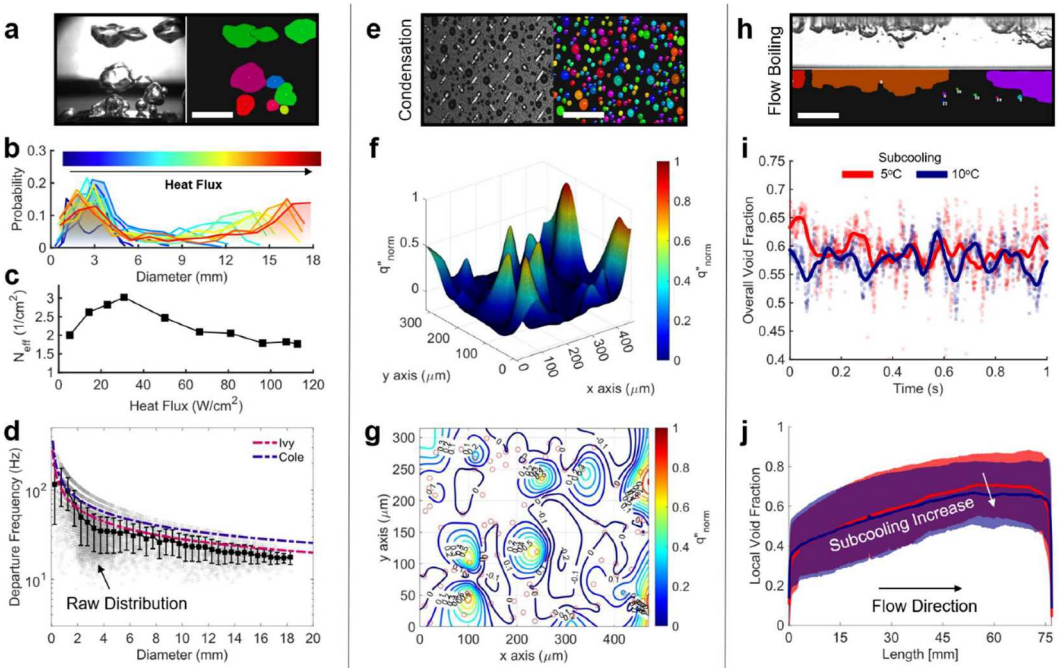

Fig. 6. Deployment of VISION-iT for various two-phase processes. For (a) pool boiling applications, the extraction of parameters such as the (b) departure diameter distribution, (c) effective nucleation site density, and (d) departure frequency is demonstrated as a function of departure diameter, where the gray scatter represents the raw data and the black markers are the averaged values over diameter bins. The departure frequency versus diameter plot is compared with previous manually verified results (pink and purple lines). The scale bar represents 5 mm. (e) Condensation on a patterned surface shows ultra-high resolution surface heat flux mappings in (f and g). The scale bar is 50 μm. (h) Flow boiling shows the evolution of the (i) instantaneous overall volume fraction and (j) local vapor void fraction for varying subcooling conditions. The scale bar is 3 mm.

Our model successfully learns how to distinguish droplets from surface patterns, which is impossible using conventional thresholding techniques. We also present flow boiling videos where vapor fractions are measured at varying scales to identify triggering mechanisms of the critical heat flux (CHF) (Fig. 6h – j). It is important to note that these are only a few of the features that VISION-iT can potentially extract. Other examples include mapping bubble rise velocity [41], droplet number distributions and densities [20], nucleation spread and distribution [20], initial nucleation site recording, nearest neighbor analysis [42], FFT-based nucleation regularity [43], and Voronoi analysis [44].

Several challenges still need to be addressed to facilitate the deployment of VISION-iT. One major challenge is generating *objective* GT trajectories for two-phase processes, which is inherently *subjective*. Hence, there is a dire need for fully autonomous systems that can intelligently generate reasonable object trajectories. In other fields, researchers have reported the use of simulated videos that match observed experimental conditions to overcome such issues [45]. Recent examples in the thermal science community include the successful reconstruction of artificial bubble images using deep neural networks [25], and the development of simulated datasets used for scientific machine learning (SciML) models [46], which are promising steps towards achieving simulated video GTs for complex two-phase processes. The development and maintenance of a global database for two-phase studies, similar to ImageNet [47], is necessary to provide researchers access to pre-trained universal detection models.

4. Conclusion

This paper introduces a state-of-the-art two-phase object tracking framework, enabling the autonomous curation of large quantities of physically descriptive features from multi-phase video data. The descriptive features acquired from this developed technique have been demonstrated to enable greater mechanistic understandings of two-phase processes by bridging the conventional gap between nucleation statistics and heat and mass transfer performances. Through systematic experiments and data-driven analysis, we identify errors that manifest during object detection and tracking processes and provide detailed documentation and guidelines for optimizing VISION-iT for custom datasets. The framework can be applied to a broad spectrum of heat fluxes for pool boiling research, as traditional investigations have been confined primarily to lower heat flux regimes. Beyond the pool boiling, we further demonstrate the potential of our framework by applying it to multiple challenging visual datasets like condensation or flow boiling, thereby showcasing its versatility in a wide spectrum of applications.

5. Methods

5.1. Model training

We train three separate Mask R-CNN models for pool boiling, dropwise condensation, and flow boiling, respectively. Each model is trained on custom-built inventories of several thousand labeled images gathered from multiple test settings. To label images, a group of annotators are individually trained on specific guidelines for each annotation project and regularly communicate with each other to maximize labeling consistency. Annotation projects are managed using a commercial annotation platform (Supervisely, San Jose, CA, USA) and by employing human-in-the-loop annotation (Fig. S1). The model generalizability is increased by diversifying the image inventory by including images with varying experimental conditions and through data augmentation techniques [16]. The data augmentation takes image transformations such as horizontal flips, brightness modification, contrast modification, and resizing to the original data, creating new, increased training data. All models are trained using stochastic gradient descent with varying learning rates. Table S3 summarizes the training parameters in detail. The pool boiling, condensation, and flow boiling models achieve test losses of 0.046, 0.11, and 0.02, respectively. We further demonstrate that our model outperforms traditional global and adaptive thresholding techniques, which are among the most used in previous literature [48], on detection performance metrics (Fig. S2). All models were fine-tuned using a single NVIDIA GeForce RTX 2070 GPU.

5.2. Video groundtruth preparation

We generate the GT of sequential images by employing human-in-the-loop annotation (Fig. S1). To validate the framework performance, we label at least 250 images per heat flux step, totaling approximately 1250 GT images. As shown in Fig. 6c, nucleation site density decreases after 50 W/cm^2, resulting in less complex bubble shapes. Therefore, we select a GT range up to 50 W/cm^2 in this study to capture the significant bubble morphology transition stages.

5.3. Side view optical measurement of pool boiling

Pool boiling experiments are conducted on a custom-built pool boiling experimental setup. The pool boiling setup is composed of a chamber, data acquisition system, copper block and four cartridge heaters. Bubble dynamics are captured using a high-speed camera (FASTCAM Mini AX50) at 2,000 fps with a light emitting diode (LED) through the optically transparent polycarbonate boiling chamber. All visualization measurements are taken at consistent focal lengths and light intensities to maintain fixed pixel-to-length ratios. Temperatures are measured from four equally-spaced K-type thermocouples embedded in the copper block. Thermal signals are processed via a data acquisition system (LabJack U6) where the obtained measurements are used to calculate the heat flux and surface temperature. The four cylindrical cartridge heaters (Omega, CIR-20191) that are inserted at the bottom of the copper block generate heat flux through a voltage transformer (Variac AC variable voltage converter). Prior to conducting the boiling test, the sample is placed and attached on the 1 cm $\times$ 1 cm copper block through soldering. Once the sample is firmly fixed on the copper block with proper polydimethylsiloxane (PDMS) sealing, the chamber is filled with the working fluid (DI water). To maintain the water temperature close to saturation, a PID-controlled guard heater is used and immersed in the water. A more detailed description of the experimental setup can be found in previous work [16,21,49].

5.4. Top view optical microscopy of water vapor condensation

A customized top-view microscopy setup is used to observe condensation behavior on biphilic surfaces [50]. The setup consists of a cold stage (TP104SC-mk2000A, Instec) that holds the sample horizontally and cools the sample surface to 5 $\pm$ 0.5 °C to condense water vapor from the laboratory ambient air having a temperature T_a = 25 $\pm$ 0.5 °C and relative humidity Φ = 55 $\pm$ 5 % (Roscid Technologies, RO120). Condensate growth behavior is recorded at 4 frames per second (fps) with a 20X objective lens (TU Plan Fluor EPI, Nikon). An LED light source (SOLA SM II Light Engine, Lumencor) is selected for illumination due to its high intensity but low power consumption (2.5 W) which minimizes the surface heating with minimal infrared emission. Moreover, the flexibility of manual control of increasing the camera exposure time and reducing the condenser aperture diaphragm opening size helps minimize local heating effects during condensation experiments. Additional details of the visualization technique can be found elsewhere [51].

5.5. Side view optical measurement of flow boiling

Single-sided heating flow boiling experiments in a rectangular channel are conducted using a flow boiling module that is part of a two-phase flow conditioning loop. The flow conditioning loop allows the capability to provide a continuous flow of the PF-5060 working fluid to

the flow boiling module and for tuning the inlet conditions that were set to provide low subcooling (near-saturated) at the module inlet. The flow module includes a rectangular channel 2.5 mm by 5 mm with single-sided heating provided on the top wall, bottom wall being insulated, and transparent side walls to allow for flow visualization access. The heated top wall, 11.6 cm in length, has 6 resistive heaters connected in parallel to simulate uniform heat flux boundary conditions. There are 7 thermocouples placed uniformly along the copper heater to measure the wall temperature and estimate the corresponding heat transfer coefficients. In addition, the inlet/outlet temperature and pressure to the flow boiling module are measured using thermocouples and pressure transducers, respectively. Flow visualization is achieved using a high-speed camera to capture the two-phase interfacial features along the heated portion of the flow channel. A fixed frame rate of 21,000 frames per second and pixel resolution of 1022×96 is used to capture the entire heated length for each test run. Illumination on the back side is provided with the use of LEDs. More details of the experiment are provided elsewhere [52,53].

CRediT authorship contribution statement

Youngjoon Suh: Conceptualization, Data curation, Investigation, Methodology, Writing – original draft, Writing – review & editing. **Sanghyeon Chang:** Data curation. **Peter Simadiris:** Investigation, Formal analysis. **Tiffany B. Inouye:** Data curation. **Muhammad Jahidul Hoque:** Investigation, Formal analysis, Writing – review & editing, Visualization. **Siavash Khodakarami:** Investigation, Formal analysis, Writing – review & editing, Visualization. **Chirag Kharangate:** Resources, Project administration, Visualization, Writing – review & editing. **Nenad Miljkovic:** Resources, Project administration, Writing – review & editing. **Yoonjin Won:** Supervision, Writing – review & editing, Funding acquisition, Project administration.

Declaration of Competing Interest

The authors declare that they have no competing financial interests that influenced the work reported in this paper.

Data availability

Data will be made available on request.

Acknowledgement

Y.S., S.C., and Y.W., gratefully acknowledge funding support from the Office of Naval Research (ONR) under Grant No. N00014-22-1-2063 and from the National Science Foundation (NSF) under CBET-TTP 2045322. J. H., S. K. and N.M. gratefully acknowledge funding support from the under grant No. N00014-21-1-2089. N.M. gratefully acknowledges funding support from the International Institute for Carbon Neutral Energy Research (WPI-I2CNER), sponsored by the Japanese Ministry of Education, Culture, Sports, Science and Technology.

Supplementary materials

Supplementary material associated with this article can be found, in the online version, at doi:10.1016/j.egyai.2023.100309.

References

[1] Cho HJ, Preston DJ, Zhu YY, Wang EN. Nanoengineered materials for liquid-vapour phase-change heat transfer. Nat Rev Mater 2017;2:16092. https://doi.org/10.1038/natrevmats.2016.92.
[2] Mousa MH, Miljkovic N, Nawaz K. Review of heat transfer enhancement techniques for single phase flows. Renew Sust Energ Rev 2021;137:110566. https://doi.org/10.1016/j.rser.2020.110566.
[3] Shoji M. Studies of boiling chaos: a review. Int J Heat Mass Transf 2004;47:1105–28. https://doi.org/10.1016/j.ijheatmasstransfer.2003.09.024.
[4] Sato Y, Niceno B. Pool boiling simulation using an interface tracking method: from nucleate boiling to film boiling regime through critical heat flux. Int J Heat Mass Tran 2018;125:876–90. https://doi.org/10.1016/j.ijheatmasstransfer.2018.04.131.
[5] Li JQ, Zhao YY, Ma JC, Fu WC, Yan X, Rabbi KF, Miljkovic N. Superior Antidegeneration Hierarchical Nanoengineered Wicking Surfaces for Boiling Enhancement. Adv Funct Mater 2021;32:2108836. https://doi.org/10.1002/adfm.202108836.
[6] Li JQ, Fu WC, Zhang BH, Zhu GH, Miljkovic N. Ultrascalable Three-Tier Hierarchical Nanoengineered Surfaces for Optimized Boiling. ACS Nano 2019;13:14080–93. https://doi.org/10.1021/acsnano.9b06501.
[7] Pham QN, Suh Y, Shao B, Won Y. Boiling heat transfer using spatially-variant and uniform microporous coatings. In: ASME 2019 International Technical Conference and Exhibition on Packaging and Integration of Electronic and Photonic Microsystems; 2019. https://doi.org/10.1115/IPACK2019-6307. V001T01A001.
[8] Suh Y, Lin CH, Gowda H, Won Y. Multiscale evaporation rate measurement using microlaser-induced fluorescence. J Electron Packaging 2020;142:031105. https://doi.org/10.1115/1.4046767.
[9] Li JQ, Kang D, Rabbi KF, Fu WC, Yan X, Fang XL, Fan LW, Miljkovic N. Liquid film-induced critical heat flux enhancement on structured surfaces. Sci Adv 2021;7:eabg4453. https://doi.org/10.1126/sciadv.abg4537.
[10] Scheckel KG, Hamon R, Jassongne L, Rivers M, Lombi E. Synchroton X-ray absorption-edge computed microtograpy imaging of thallium compartmentalization in Iberis intermedia (vol 290, pg 51, 2007). Plant Soil 2007;294:305–6. https://doi.org/10.1007/s11104-006-9102-7.
[11] Cho HJ, Mizerak JP, Wang EN. Turning bubbles on and off during boiling using charged surfactants. Nat Commun 2015;6:8599. https://doi.org/10.1038/ncomms9599.
[12] Lee J, Mudawar I, Hasan MM, Nahra HK, Mackey JR. Experimental and computational investigation of flow boiling in microgravity. Int J Heat Mass Tran 2022;183:122237. https://doi.org/10.1016/j.ijheatmasstransfer.2021.122237.
[13] Attinger D, Frankiewicz C, Betz AR, Schutzius TM, Ganguly R, Das A, Kim CJ, Megaridis CM. Surface engineering for phase change heat transfer: a review. MRS Energy Sustain 2014;1(E4). https://doi.org/10.1557/mre.2014.9.
[14] Mohanty RL, Das MK. A critical review on bubble dynamics parameters influencing boiling heat transfer. Renew Sust Energ Rev 2017;78:466–94. https://doi.org/10.1016/j.rser.2017.04.092.
[15] Chatpun S, Watanabe M, Shoji M. Experimental study on characteristics of nucleate pool boiling by the effects of cavity arrangement. Exp Therm Fluid Sci 2004;29:33–40. https://doi.org/10.1016/j.expthermflusci.2004.01.007.
[16] Suh Y, Bostanabad R, Won Y. Deep learning predicts boiling heat transfer. Sci Rep 2021;11:5622. https://doi.org/10.1038/s41598-021-85150-4.
[17] Jin Y, Shirvan K. Study of the film boiling heat transfer and two-phase flow interface behavior using image processing. Int J Heat Mass Transf 2021;177:121517. https://doi.org/10.1016/j.ijheatmasstransfer.2021.121517.
[18] Maurus R, Ilchenko V, Sattelmayer T. Study of the bubble characteristics and the local void fraction in subcooled flow boiling using digital imaging and analysing techniques. Exp Therm Fluid Sci 2002;26:147–55. https://doi.org/10.1016/S0894-1777(02)00121-8.
[19] Surtaev A, Serdyukov V, Zhou JJ, Pavlenko A, Tumanov V. An experimental study of vapor bubbles dynamics at water and ethanol pool boiling at low and high heat fluxes. Int J Heat Mass Transf 2018;126:297–311. https://doi.org/10.1016/j.ijheatmasstransfer.2018.06.001.
[20] Suh Y, Lee J, Simadiris P, Yan X, Sett S, Li LN, Rabbi KF, Miljkovic N, Won Y. A Deep learning perspective on dropwise condensation. Adv Sci 2021;8:2170153. https://doi.org/10.1002/advs.202170153.
[21] Lee J, Suh Y, Kuciej M, Simadiris P, Barako M, Won Y. Computer vision-assisted investigation of boiling heat transfer on segmented nanowires with vertical wettability. Nanoscale 2022;14:13078–89. https://doi.org/10.1039/D2NR02447K.
[22] O'Mahony N, Campbell S, Carvalho A, Harapanahalli S, Hernandez GV, Krpalkova L, Riordan D, Walsh J. Deep learning vs. traditional computer vision, Science and information conference. Springer 2019:128–44. https://doi.org/10.1007/978-3-030-17795-9_10.
[23] Hobold GM, da Silva AK. Visualization-based nucleate boiling heat flux quantification using machine learning. Int J Heat Mass Transf 2019;134:511–20. https://doi.org/10.1016/j.ijheatmasstransfer.2018.12.170.
[24] Hobold GM, da Silva AK. Automatic detection of the onset of film boiling using convolutional neural networks and Bayesian statistics. Int J Heat Mass Transf 2019;134:262–70. https://doi.org/10.1016/j.ijheatmasstransfer.2018.12.070.
[25] Rokoni A, Zhang L, Soori T, Hu H, Wu T, Sun Y. Learning new physical descriptors from reduced-order analysis of bubble dynamics in boiling heat transfer. Int J Heat Mass Transf 2022;186:122501. https://doi.org/10.1016/j.ijheatmasstransfer.2021.122501.
[26] Hughes MT, Kini G, Garimella S. Status, challenges, and potential for machine learning in understanding and applying heat transfer phenomena. J Heat Trans-T Asme 2021;143:120802. https://doi.org/10.1115/1.4052510.
[27] Ren S, He K, Girshick R, Sun J. Faster r-cnn: towards real-time object detection with region proposal networks. Adv Neural Inf Process Syst 2015:28.
[28] Khodakarami S, Rabbi KF, Suh Y, Won Y, Miljkovic N. Machine learning enabled condensation heat transfer measurement. Int J Heat Mass Transf 2022;194:123016. https://doi.org/10.1016/j.ijheatmasstransfer.2022.123016.
[29] He K, Gkioxari G, Dollár P, Girshick R. Mask r-cnn. In: Proceedings of the IEEE international conference on computer vision; 2017. p. 2961–9.

[30] Allan D, Caswell T, Keim N, van der Wel C. trackpy: trackpy v0. 3.2. Zenodo 2016.
[31] Tsai HF, Gajda J, Sloan TFW, Rares A, Shen AQ. Usiigaci: instance-aware cell tracking in stain-free phase contrast microscopy enabled by machine learning. Softwarex 2019;9:230–7. https://doi.org/10.1016/j.softx.2019.02.007.
[32] Upot NV, Mahvi A, Fazle Rabbi K, Li J, Jacobi AM, Miljkovic N. Scalable and resilient etched matallic micro- and nanostructured surfaces for enhanced flow boiling. ACS Appl. Nano Mater. 2021;4:6648–58. https://doi.org/10.1021/acsanm.1c00524.
[33] Van der Walt S, Schönberger JL, Nunez-Iglesias J, Boulogne F, Warner JD, Yager N, Gouillart E, Yu T. scikit-image: image processing in Python. PeerJ 2014;2:e453.
[34] Crocker JC, Grier DG. Methods of digital video microscopy for colloidal studies. J Colloid Interf Sci 1996;179:298–310. https://doi.org/10.1006/jcis.1996.0217.
[35] Kim Y, Park H. Deep learning-based automated and universal bubble detection and mask extraction in complex two-phase flows. Sci Rep-Uk 2021;11:8940. https://doi.org/10.1038/s41598-021-88334-0.
[36] Sundaramoorthi G., Wang T.E., Translation insensitive cnns. arXiv preprint arXiv: 1911.11238. 2019 https://doi.org/10.48550/arXiv.1911.11238.
[37] Fawcett T. An introduction to ROC analysis. Pattern Recogn Lett 2006;27:861–74. https://doi.org/10.1016/j.patrec.2005.10.010.
[38] Leal-Taixé L., Milan A., Schindler K., Cremers D., Reid I., Roth S., Tracking the trackers: an analysis of the state of the art in multiple object tracking. *arXiv preprint arXiv:1704.02781*. 2017 https://doi.org/10.48550/arXiv.1704.02781.
[39] Luo W, Xing J, Milan A, Zhang X, Liu W, Kim TK. Multiple object tracking: a literature review. Artif Intell 2021;293:103448. https://doi.org/10.1016/j.artint.2020.103448.
[40] Hoang NH, Song CH, Chu IC, Euh DJ. A bubble dynamics-based model for wall heat flux partitioning during nucleate flow boiling. Int J Heat Mass Tran 2017;112:454–64. https://doi.org/10.1016/j.ijheatmasstransfer.2017.04.128.
[41] Park SH, Park C, Lee J, Lee B. A Simple parameterization for the rising velocity of bubbles in a liquid pool. Nucl Eng Technol 2017;49:692–9. https://doi.org/10.1016/j.net.2016.12.006.
[42] Zhang LN, Iwata R, Zhao L, Gong S, Lu ZM, Xu ZY, Zhong Y, Zhu JL, Cruz S, Wilke KL, Cheng P, Wang EN. Nucleation site distribution probed by phase-enhanced environmental scanning electron microscopy. Cell Rep Phys Sci 2020;1:100262. https://doi.org/10.1016/j.xcrp.2020.100262.
[43] Mandsberg NK, Taboryski R. Spatial control of condensation on chemically homogeneous pillar-built surfaces. Langmuir 2017;33:5197–203. https://doi.org/10.1021/acs.langmuir.7b01159.
[44] Suh Y, Pham Q, Shao BW, Won Y. The control of colloidal grain boundaries through evaporative vertical self-assembly. Small 2019;15:1804523. https://doi.org/10.1002/smll.201804523.
[45] Newby JM, Schaefer AM, Lee PT, Forest MG, Lai SK. Convolutional neural networks automate detection for tracking of submicron-scale particles in 2D and 3D. P Natl Acad Sci USA 2018;115:9026–31. https://doi.org/10.1073/pnas.1804420115.
[46] Hassan S.M.S., Feeney A., Dhruv A., Suh Y., Kim J., Ryu J., Won Y., Chandramowlishwaran A., BubbleML: a multi-physics dataset and benchmarks for machine learning. *arXiv preprint arXiv:2307.14623*. 2023 https://arxiv.org/abs/2307.14623.
[47] Deng J, Dong W, Socher R, Li LJ, Li K, Fei-Fei L. Imagenet: a large-scale hierarchical image database. In: 2009 IEEE conference on computer vision and pattern recognition. IEEE; 2009. p. 248–55. https://doi.org/10.1109/CVPR.2009.5206848.
[48] Martin H, Barati SB, Pinoli JC, Valette S, Gavet Y. Segmentation of gray scale images of dropwise condensation on textured surfaces. Int J Comput Inf Eng 2018;12:753–61. https://doi.org/10.5281/zenodo.1474614.
[49] Lee J., Suh Y., Kuciej M., Simadiris P., Barako M.T., Won Y., Deep vision-inspired bubble dynamics on hybrid nanowires with dual wettability. arXiv preprint arXiv: 2202.09417. 2022 https://doi.org/10.48550/arXiv.2202.09417.
[50] Kim MK, Cha H, Birbarah P, Chavan S, Zhong C, Xu YH, Miljkovic N. Enhanced jumping-droplet departure. Langmuir 2015;31:13452–66. https://doi.org/10.1021/acs.langmuir.5b03778.
[51] Chavan S, Cha H, Orejon D, Nawaz K, Singla N, Yeung YF, Park D, Kang DH, Chang YJ, Takata Y, Miljkovic N. Heat transfer through a condensate droplet on hydrophobic and nanostructured superhydrophobic surfaces. Langmuir 2016;32:7774–87. https://doi.org/10.1021/acs.langmuir.6b01903.
[52] Kharangate CR, O'Neill LE, Mudawar I, Hasan MM, Nahra HK, Balasubramaniam R, Hall NR, Macner AM, Mackey JR. Flow boiling and critical heat flux in horizontal channel with one-sided and double-sided heating. Int J Heat Mass Tran 2015;90:323–38. https://doi.org/10.1016/j.ijheatmasstransfer.2015.06.073.
[53] Kharangate CR, O'Neill LE, Mudawar I, Hasan MM, Nahra HK, Balasubramaniam R, Hall NR, Macner AM, Mackey JR. Effects of subcooling and two-phase inlet on flow boiling heat transfer and critical heat flux in a horizontal channel with one-sided and double-sided heating. Int J Heat Mass Tran 2015;91:1187–205. https://doi.org/10.1016/j.ijheatmasstransfer.2015.08.059.